

# Self-Assembly of Surface-Functionalized $\text{Ag}_{1.8}\text{Mn}_8\text{O}_{16}$ Nanorods with Reduced Graphene Oxide Nanosheets as an Efficient Bifunctional Electrocatalyst for Rechargeable Zinc-Air Batteries

Guojun Du,<sup>[a, b, d]</sup> Yun Zong,<sup>\*,[c]</sup> Xiaogang Liu,<sup>[b, c]</sup> and Zhaolin Liu<sup>\*,[c]</sup>

**Abstract:** Bifunctional electrocatalysts play a key role in the performance of rechargeable metal-air batteries. Herein, we report a hybrid catalyst,  $\text{Ag}_{1.8}\text{Mn}_8\text{O}_{16}/\text{rGO}$ , self-assembled by  $\text{Ag}_{1.8}\text{Mn}_8\text{O}_{16}$  nanorods and reduced graphene oxide (rGO) nanosheets through electrostatic attraction. The hybrid catalyst exhibits a better oxygen reduction reaction (ORR) and oxygen evolution reaction (OER) activity than commercial

Pt/C in alkaline medium. When employed as an air-cathode catalyst in Zn-air cells, the hybrids enabled higher and more stable output voltage and better durability of the cells, benefitting from the improved electrode conductivity, larger surface area, and synergetic coupling as a result of its high structural integrity.

## Introduction

Rapid development of global economy demands more sustainable energy supply, stimulating intense research on highly efficient, environmentally benign, and cost-effective alternative energy conversion and storage systems.<sup>[1–3]</sup> The renewable-energy technologies such as Zn-air batteries are excellent candidates, thanks to their high energy density, good safety, and environmental benignity. The performance of Zn-air battery is mainly determined by the electrochemical reaction of air electrode. The chemical processes involve the mass transfer on the interface in multi-phase system. Moreover, the reaction kinetics, including the ORR during the charging process and the OER during the discharging process, is the main reason for high polarization and poor cycling performance of Zn-air batteries. The active bifunctional catalyst can accelerate the reaction kinetics, decrease the overpotential between charging and discharging process, and thus improve the performance of Zn-air batteries.<sup>[4–6]</sup>

To enable high-performance Zn-air batteries, a key is to develop efficient yet low-cost catalysts for oxygen reduction reaction (ORR) and oxygen evolution reaction (OER).<sup>[4–7]</sup> Pt group metal and oxides are good model catalysts for fundamental studies and as benchmarks,<sup>[8–10]</sup> while it is a natural choice for practical applications to turn to materials of high abundance, such as transition metal oxides<sup>[11–18]</sup> and carbonaceous materials.<sup>[19–25]</sup>

An interesting candidate for bifunctional catalysts towards ORR and OER is Ag-hollandite manganese oxide ( $\text{Ag}_{1.8}\text{Mn}_8\text{O}_{16}$ ) studied in ethanol oxidation catalysis,<sup>[26]</sup> emission control,<sup>[27]</sup> and as electrode material for lithium-ion secondary batteries.<sup>[28]</sup> It possesses the merits of low cost, high abundance, low toxicity and multiple valence state, but lacks good electron transport required for high catalytic activity. Compositing with conductive carbonaceous materials is a viable solution, where highly conductive graphene stands out for its additional merits of high thermal and chemical stability, accessible large specific surface area, and good mechanical properties which are keys to practical applications.<sup>[29–32]</sup> Moreover, synergistic coupling between metal oxides and graphene is proven to benefit the ORR and OER activities.<sup>[33–36]</sup> Liang and co-workers reported rGO-supported  $\text{Co}_3\text{O}_4$  nanocrystals with high ORR and OER catalytic activity.<sup>[33]</sup> Similarly, Liu et al. demonstrated promising ORR and OER catalysis using nanohybrid of  $\text{LaCoO}_3/\text{N-doped reduced graphene oxide}$  ( $\text{LaCoO}_3/\text{N-rGO}$ ).<sup>[34]</sup> Loading of catalysts onto carbon support in these works was more of spontaneous deposition.

We hence anticipate that the combination of  $\text{Ag}_{1.8}\text{Mn}_8\text{O}_{16}$  and rGO could lead to the production of bifunctional electrocatalysts with substantially improved electrocatalytic activity for both ORR and OER. The combination of one-dimensional (1-D)  $\text{Ag}_{1.8}\text{Mn}_8\text{O}_{16}$  nanorods and two-dimensional (2-D) rGO offers several advantages: (i) better charge transport ability, (ii) low mass loading, (iii) better mass transport of the solvated ions, and (iv) better mechanical toughness.<sup>[16]</sup>

In this work, we report directed formation of  $\text{Ag}_{1.8}\text{Mn}_8\text{O}_{16}/\text{rGO}$  via a self-assembling process. Surface functionalized

[a] Dr. G. Du  
College of Chemistry and Molecular Engineering  
Peking University  
Beijing 100871 (P. R. China)

[b] Dr. G. Du, Prof. X. Liu  
Department of Chemistry  
National University of Singapore  
3 Science Drive 3, 117543 (Singapore)

[c] Dr. Y. Zong, Prof. X. Liu, Dr. Z. Liu  
Institute of Materials Research and Engineering (IMRE)  
Agency for Science, Technology and Research (A\*STAR)  
2 Fusionopolis Way, Innovis, #08-03, 138634 (Singapore)  
E-mail: Zong\_Yun@hq.a-star.edu.sg  
zl-liu@imre.a-star.edu.sg

[d] Dr. G. Du  
Department of Environment and Materials Engineering  
Jiangyin Polytechnic College  
Wuxi Shi, Jiangyin 214405 (P. R. China)

Supporting information for this article is available on the WWW under <https://doi.org/10.1002/asia.202100940>

This manuscript is part of a special collection on Metals in Functional Materials and Catalysis.

$\text{Ag}_{1.8}\text{Mn}_8\text{O}_{16}$  nanorods with positive charges bind with rGO nanosheets with opposite charges on their surfaces through electrostatic attractions. The resultant  $\text{Ag}_{1.8}\text{Mn}_8\text{O}_{16}/\text{rGO}$  nanohybrids show good activities in ORR and OER catalysis, outperforming commercial Pt/C as cathode electrocatalyst in rechargeable Zn-air batteries.

## Results and Discussion

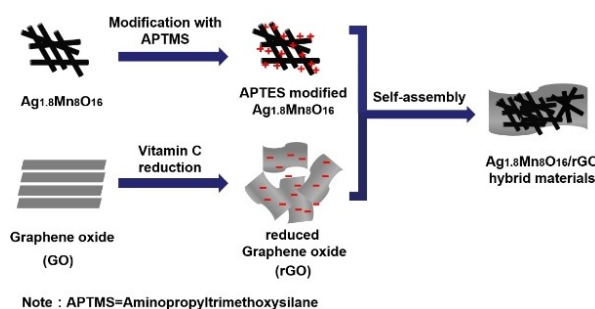
### Synthesis, morphological, structural characterization

The preparation of the  $\text{Ag}_{1.8}\text{Mn}_8\text{O}_{16}/\text{rGO}$  is schematically illustrated in Scheme 1.  $\text{Ag}_{1.8}\text{Mn}_8\text{O}_{16}$  nanorods were hydrothermally prepared, followed by surface grafting of aminopropyltrimethoxysilane (APTMS) to introduce positive charges. rGO nanosheets dispersion was prepared by reducing GO using Vitamin C. The APTMS-functionalized  $\text{Ag}_{1.8}\text{Mn}_8\text{O}_{16}$  nanorods were then mixed with oppositely charged rGO nanosheets to allow for self-assembling to produce  $\text{Ag}_{1.8}\text{Mn}_8\text{O}_{16}/\text{rGO}$  via electrostatic attraction. The Zeta potentials of rGO and APTMS modified  $\text{Ag}_{1.8}\text{Mn}_8\text{O}_{16}$  are  $-21$  mV and  $+28$  mV, respectively. According to the Zeta potential, rGO and APTMS modified  $\text{Ag}_{1.8}\text{Mn}_8\text{O}_{16}$  can be self-assembled by electrostatic attractions.

The X-ray diffraction patterns of  $\text{Ag}_{1.8}\text{Mn}_8\text{O}_{16}$ , rGO and  $\text{Ag}_{1.8}\text{Mn}_8\text{O}_{16}/\text{rGO}$  are presented in Figure 1a. All major diffraction peaks of  $\text{Ag}_{1.8}\text{Mn}_8\text{O}_{16}$  match well with the tetragonal structure (JCPDS No. 77-1987;  $a = 9.725$  Å,  $c = 2.885$  Å; space group: I4/m) of pure silver manganese oxide. The absence of any other characteristic peaks suggests high phase purity for the as-prepared  $\text{Ag}_{1.8}\text{Mn}_8\text{O}_{16}$ . rGO shows only one broad peak centered at  $24.3^\circ$ , corresponding to (002) crystal plane of graphene. The diffraction peaks of  $\text{Ag}_{1.8}\text{Mn}_8\text{O}_{16}/\text{rGO}$  match those of

$\text{Ag}_{1.8}\text{Mn}_8\text{O}_{16}$  and no show of rGO diffraction peak is likely due to the strong coupling between  $\text{Ag}_{1.8}\text{Mn}_8\text{O}_{16}$  and rGO. Nitrogen adsorption-desorption isotherms (Figure 1b) give specific surface areas of 45, 142, and  $76 \text{ m}^2 \text{ g}^{-1}$  for  $\text{Ag}_{1.8}\text{Mn}_8\text{O}_{16}$ , rGO, and  $\text{Ag}_{1.8}\text{Mn}_8\text{O}_{16}/\text{rGO}$  hybrids, respectively. The increased specific surface area  $\text{Ag}_{1.8}\text{Mn}_8\text{O}_{16}/\text{rGO}$  as compared to that of  $\text{Ag}_{1.8}\text{Mn}_8\text{O}_{16}$  further approves the successful incorporation of rGO which has a notably large specific surface area. The content of rGO in the hybrids, based on the TGA data (Figure S1), is estimated to be 34 wt%, similar to that added at the start of synthesis.

TEM and HRTEM images of  $\text{Ag}_{1.8}\text{Mn}_8\text{O}_{16}$  and  $\text{Ag}_{1.8}\text{Mn}_8\text{O}_{16}/\text{rGO}$  are shown in Figure 2. The reduced graphene oxides sheets are ultrathin and wrinkled (Figure 2a, b), and  $\text{Ag}_{1.8}\text{Mn}_8\text{O}_{16}$  are nanorods with average diameter of about 25 nm and length up to 2  $\mu\text{m}$  (Figure 2c). In the HRTEM image (Figure 2d) the lattice spacing is 0.276 nm for  $\text{Ag}_{1.8}\text{Mn}_8\text{O}_{16}$  nanorods, corresponding to the (101) planes of tetragonal  $\text{Ag}_{1.8}\text{Mn}_8\text{O}_{16}$ . TEM image of  $\text{Ag}_{1.8}\text{Mn}_8\text{O}_{16}/\text{rGO}$  hybrids (Figure 2e) shows nanorods ( $\text{Ag}_{1.8}\text{Mn}_8\text{O}_{16}$ ) attached to nanosheets (rGO), and no free nanorod is identifiable. HRTEM image features a single nanorod on rGO nanosheet (Figure 2f), where the lattice spacing of 0.343 nm is from the (220) planes of tetragonal  $\text{Ag}_{1.8}\text{Mn}_8\text{O}_{16}$ . The TEM (Figure 2e) and SEM images (Figure S2) unanimously approve well-integrated nanorods/nanosheets structure of  $\text{Ag}_{1.8}\text{Mn}_8\text{O}_{16}/\text{rGO}$ . With improved interface contact, the hybrid catalyst is expected to exhibit excellent electrochemical activity and stability. The mass transfer and electron transfer can be



Scheme 1. Synthetic process of the  $\text{Ag}_{1.8}\text{Mn}_8\text{O}_{16}/\text{rGO}$  hybrids.

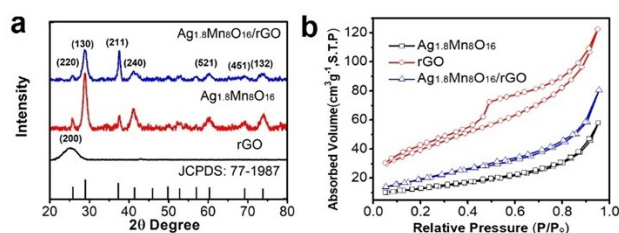


Figure 1. a) XRD patterns and b) the  $\text{N}_2$  adsorption/desorption isotherm of the rGO,  $\text{Ag}_{1.8}\text{Mn}_8\text{O}_{16}$  and  $\text{Ag}_{1.8}\text{Mn}_8\text{O}_{16}/\text{rGO}$  hybrids.

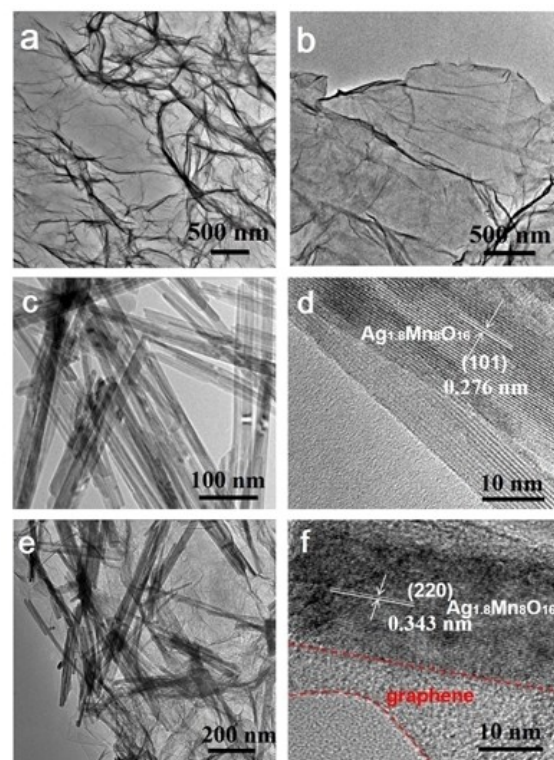


Figure 2. TEM images of rGO (a-b);  $\text{Ag}_{1.8}\text{Mn}_8\text{O}_{16}$  (c) and  $\text{Ag}_{1.8}\text{Mn}_8\text{O}_{16}/\text{rGO}$  hybrids (e). HRTEM images of the  $\text{Ag}_{1.8}\text{Mn}_8\text{O}_{16}$  (d) and  $\text{Ag}_{1.8}\text{Mn}_8\text{O}_{16}/\text{rGO}$  hybrids (f).

greatly improved due to the increasing interface contact. In addition, the novel nanorod/nanosheet structure have better mechanical toughness, which is beneficial for the enhancement of catalyst activity.<sup>[2,4]</sup>

The composition and chemical states of  $\text{Ag}_{1.8}\text{Mn}_8\text{O}_{16}/\text{rGO}$  hybrids are examined using X-ray photoelectron spectroscopy (XPS). The presence of Ag, Mn, O and C is confirmed (Figure S3). The binding energies of Ag (3d5/2) and Ag (3d3/2) peaks centered at 366.8 and 372.7 eV (Figure 3a), respectively, suggest  $\text{Ag}^+$  as the species in the nanorods,<sup>[37]</sup> differentiating from  $\text{Ag}^0$  with Ag (3d5/2) at 368.2 eV.<sup>[38]</sup> The binding energies of Mn (2p3/2) and Mn (2p1/2) centered at 641.6 and 653.2 eV (Figure 3b), respectively, can be attributed to a mixture of  $\text{Mn}^{4+}$  and  $\text{Mn}^{3+}$  species. This is in good agreement with those of Mn (2p3/2) and Mn (2p1/2) in  $\text{Ag}_{1.8}\text{Mn}_8\text{O}_{16}$  as reported previously.<sup>[37]</sup> Four types of oxygen species are identified (Figure 3c), with the peaks at 529.1, 530.2, 531.4 and 532.5 eV ascribed to lattice oxygen (Mn–O), O=C–O on rGO, surface adsorbed molecular oxygen, and oxygen in adsorbed molecular water, respectively.<sup>[39]</sup> The  $\text{O}_{\text{ads}}$  species are readily activated by the oxygen vacancies in  $\text{Ag}_{1.8}\text{Mn}_8\text{O}_{16}$  during the ORR.<sup>[40]</sup> The deconvolution of C1s XPS spectrum (Figure 3d) gives three peaks, with the symmetrical one at 285.0 eV assigned to C–C of rGO. The other two peaks at 286.2 and 288.8 eV associate with C–O and C=O, respectively. Similar assignment was reported previously.<sup>[39]</sup>

### Electrocatalytic activity on ORR and OER

The ORR and OER catalytic activities were evaluated by linear sweep voltammetry with a rotating disk electrode using a three-electrode system. In details, catalyst activity toward the ORR was evaluated in oxygen-saturated electrolyte solution from 0.2 to  $-0.8$  V. The catalytic performance for OER was measured in the electrolyte solution from 0.2 to 1.0 V. The rotation rate is 2000 rpm and the scan rate is  $5 \text{ mVs}^{-1}$ . As

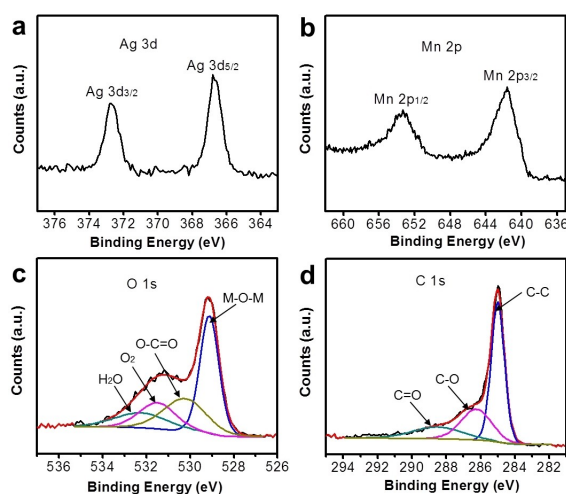


**Figure 3.** High resolution XPS analysis of Ag(3d) (a), Mn(2p) (b), O(1 s) (c) and C(1 s) (d) for the  $\text{Ag}_{1.8}\text{Mn}_8\text{O}_{16}/\text{rGO}$  hybrids.

shown in Figure 4a, the onset potential for  $\text{Ag}_{1.8}\text{Mn}_8\text{O}_{16}/\text{rGO}$  hybrids is detected at 0.18 V, whereas it is 0.06 V and 0.14 V for rGO and  $\text{Ag}_{1.8}\text{Mn}_8\text{O}_{16}$  nanorods, respectively. In addition, the onset potential of commercial Pt/C is 0.17 V, tested following the same procedures. The ORR half-wave potential for  $\text{Ag}_{1.8}\text{Mn}_8\text{O}_{16}/\text{rGO}$  hybrids, rGO,  $\text{Ag}_{1.8}\text{Mn}_8\text{O}_{16}$  nanorods and Pt/C is  $-0.21$  V,  $-0.26$  V,  $-0.36$  V and  $-0.11$  V, respectively. At  $-0.8$  V, the  $\text{Ag}_{1.8}\text{Mn}_8\text{O}_{16}$ , rGO and  $\text{Ag}_{1.8}\text{Mn}_8\text{O}_{16}/\text{rGO}$  afford an ORR current density of 5.7, 6.4 and  $8.4 \text{ mA cm}^{-2}$ , respectively. The ORR current density of the hybrid is even higher than that of commercial Pt/C ( $7.5 \text{ mA cm}^{-2}$ ). Although the ORR half-wave potential of  $\text{Ag}_{1.8}\text{Mn}_8\text{O}_{16}/\text{rGO}$  hybrids is more negative than that of commercial Pt/C, the more positive onset potential and larger cathodic current suggest higher catalytic activities for  $\text{Ag}_{1.8}\text{Mn}_8\text{O}_{16}/\text{rGO}$  hybrids as compared to  $\text{Ag}_{1.8}\text{Mn}_8\text{O}_{16}$  or rGO, and the commercial Pt/C. OER current density at 1.0 V for  $\text{Ag}_{1.8}\text{Mn}_8\text{O}_{16}$  nanorods, rGO,  $\text{Ag}_{1.8}\text{Mn}_8\text{O}_{16}/\text{rGO}$  hybrids, and Pt/C are measured to be 11.5, 17.0, 18.9 and  $18.6 \text{ mA cm}^{-2}$ , respectively (Figure 4b). The results show that the OER activity of  $\text{Ag}_{1.8}\text{Mn}_8\text{O}_{16}$  nanorods is notably improved by incorporating rGO to form  $\text{Ag}_{1.8}\text{Mn}_8\text{O}_{16}/\text{rGO}$ .

To further understand the enhanced performance in  $\text{Ag}_{1.8}\text{Mn}_8\text{O}_{16}/\text{rGO}$  hybrid, ORR activities of  $\text{Ag}_{1.8}\text{Mn}_8\text{O}_{16}/\text{GO}$  and mechanical mixture of bare- $\text{Ag}_{1.8}\text{Mn}_8\text{O}_{16}$  nanorods and rGO (mix- $\text{Ag}_{1.8}\text{Mn}_8\text{O}_{16}/\text{rGO}$ ), were also studied. The mix- $\text{Ag}_{1.8}\text{Mn}_8\text{O}_{16}/\text{rGO}$  and  $\text{Ag}_{1.8}\text{Mn}_8\text{O}_{16}/\text{GO}$  were prepared following the same procedure except no surface functionalization of  $\text{Ag}_{1.8}\text{Mn}_8\text{O}_{16}$  for the former and no reduction of GO for the latter. At  $-0.8$  V the ORR current density of  $\text{Ag}_{1.8}\text{Mn}_8\text{O}_{16}/\text{GO}$ , mix- $\text{Ag}_{1.8}\text{Mn}_8\text{O}_{16}/\text{rGO}$  and  $\text{Ag}_{1.8}\text{Mn}_8\text{O}_{16}/\text{rGO}$  is 2.2, 6.8 and  $8.4 \text{ mA cm}^{-2}$ , respectively (Figure 4c). The poorest performance of  $\text{Ag}_{1.8}\text{Mn}_8\text{O}_{16}/\text{GO}$  is

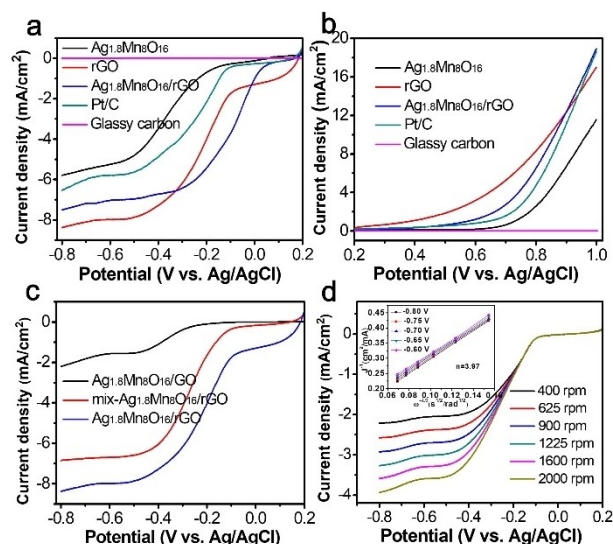


**Figure 4.** a) ORR polarization and b) OER polarization curves of the  $\text{Ag}_{1.8}\text{Mn}_8\text{O}_{16}$ , rGO,  $\text{Ag}_{1.8}\text{Mn}_8\text{O}_{16}/\text{rGO}$  hybrids, commercial Pt/C and glassy carbon. c) ORR polarization curves of the  $\text{Ag}_{1.8}\text{Mn}_8\text{O}_{16}/\text{GO}$ , mix- $\text{Ag}_{1.8}\text{Mn}_8\text{O}_{16}/\text{rGO}$  and  $\text{Ag}_{1.8}\text{Mn}_8\text{O}_{16}/\text{rGO}$  hybrids. The catalyst load is  $0.5 \text{ mg cm}^{-2}$ . d) Rotating-disk voltammogram of  $\text{Ag}_{1.8}\text{Mn}_8\text{O}_{16}/\text{rGO}$  hybrids in  $\text{O}_2$ -saturated 0.1 M KOH at a sweep rate of  $5 \text{ mVs}^{-1}$  and different rotation rates. The inset shows the corresponding Koutecky-Levich plot ( $J^{-1}$  versus  $\omega^{-0.5}$ ) at different potentials. The catalyst load is  $0.1 \text{ mg cm}^{-2}$ .



due to low electrical conductivity of GO, and use of its conductive counterpart, rGO, improves the catalytic activity.  $\text{Ag}_{1.8}\text{Mn}_8\text{O}_{16}/\text{rGO}$  is also superior to mix- $\text{Ag}_{1.8}\text{Mn}_8\text{O}_{16}/\text{rGO}$  in ORR activity, where the enhancement of catalytic activity arises from synergetic chemical coupling when  $\text{Ag}_{1.8}\text{Mn}_8\text{O}_{16}$  is closely attached onto rGO. Moreover, high surface area generally provides more active sites for ORR and hence enhances the catalytic performance.  $\text{Ag}_{1.8}\text{Mn}_8\text{O}_{16}/\text{rGO}$  with higher electric conductivity and nearly doubled surface area that of  $\text{Ag}_{1.8}\text{Mn}_8\text{O}_{16}$  (Figure 1b) naturally give the former improved ORR activity.

The ORR kinetics was studied using rotating-disk electrode (RDE) tests at different rotating speeds. Figure 4d shows the ORR curves of in 0.1 M KOH at a sweep rate of  $5 \text{ mV s}^{-1}$  and different rotation rates. With increased rotation rate, the diffusion limiting current density rises due to the improved  $\text{O}_2$  diffusion. The corresponding Koutecky-Levich plots (inset of Figure 4d) shows good linearity and parallelism of the fitting lines, suggesting a first-order reaction kinetics toward the concentration of dissolved oxygen.<sup>[33]</sup> The electron transfer number ( $n$ ) was calculated to be about 3.97 at  $-0.60 \sim -0.80 \text{ V}$  from the slopes of Koutecky-Levich plots (illustration in the Experimental Section). This shows that  $\text{Ag}_{1.8}\text{Mn}_8\text{O}_{16}/\text{rGO}$  favours 4 electron-transfer in ORR, similar to a high-quality commercial Pt/C catalyst measured in the same 0.1 M KOH electrolyte.<sup>[33]</sup> The 4 electron-transfer reaction pathway is preferred for ORR due to the higher efficiency and the mitigated detrimental peroxide species.<sup>[6]</sup>

### Zn-air battery performance

Zn-air cells were built using  $\text{Ag}_{1.8}\text{Mn}_8\text{O}_{16}/\text{rGO}$  or  $\text{Ag}_{1.8}\text{Mn}_8\text{O}_{16}$  nanorods as air-cathode catalyst to evaluate their performance in batteries. A typical polarization curve ( $V \sim i$ ) and the corresponding power density plot are shown in Figure 5a. With  $\text{Ag}_{1.8}\text{Mn}_8\text{O}_{16}/\text{rGO}$ -based electrode the cell delivers a current density of up to  $\sim 39 \text{ mA cm}^{-2}$  at a discharging voltage of 1 V, higher than that of its counterpart with  $\text{Ag}_{1.8}\text{Mn}_8\text{O}_{16}$ -based electrode. The peak power density of the former is  $42 \text{ mW cm}^{-2}$  at  $25^\circ\text{C}$ , superior to zinc-air cells with similar electrode catalysts of  $\text{MnO}_2/\text{Co}_3\text{O}_4$  ( $33 \text{ mW cm}^{-2}$ )<sup>[16]</sup> and for  $\text{PbMnO}_x$  ( $35 \text{ mW cm}^{-2}$ )<sup>[41]</sup> tested at similar conditions.

According to the discharge curves of primary Zn-air batteries with  $\text{Ag}_{1.8}\text{Mn}_8\text{O}_{16}/\text{rGO}$  as the cathode catalyst under continuous discharge until complete consumption of Zn at  $20 \text{ mA cm}^{-2}$  (Figure S4), the specific capacity normalized to the mass of consumed Zn was  $594 \text{ mAh g}^{-1}$ , corresponding to a high energy density  $683 \text{ Wh kg}^{-1}$ .

The zinc-air cells were cycled by discharging and charging (10 min each in a cycle) at  $20 \text{ mA cm}^{-2}$  using recurrent galvanic pulses method, and the results are shown in Figure 5b. The lower charge voltage plateau and higher discharge voltage plateau are seen for the cell with  $\text{Ag}_{1.8}\text{Mn}_8\text{O}_{16}/\text{rGO}$ -based electrode as compared to its counterpart using  $\text{Ag}_{1.8}\text{Mn}_8\text{O}_{16}$ -based electrode. The deterioration of charge potential and discharge potential after 100 cycles is less serious for the

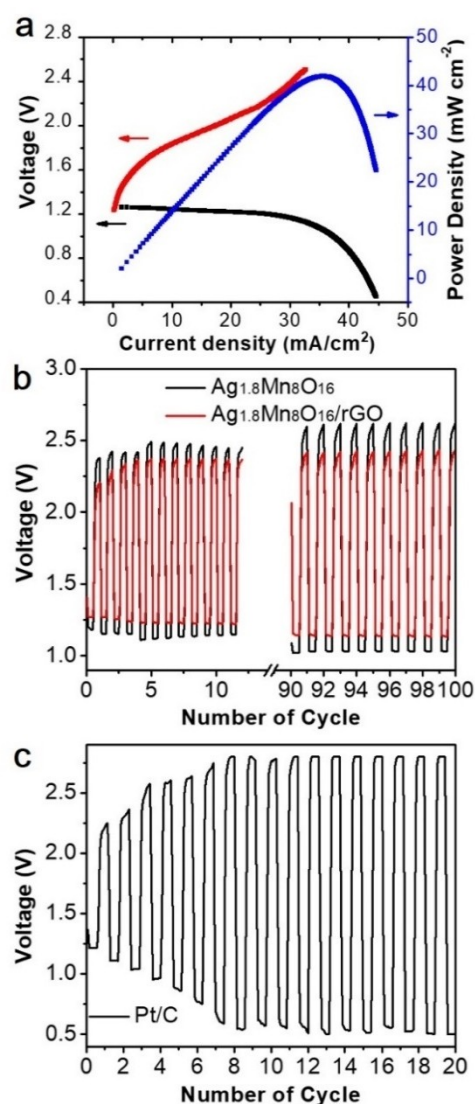


**Figure 5.** a) Discharge and charge polarization curves ( $V \sim i$ ) and the corresponding power density plot of the  $\text{Ag}_{1.8}\text{Mn}_8\text{O}_{16}/\text{rGO}$  hybrids. b) Cycling charge-discharge performance of the batteries using the  $\text{Ag}_{1.8}\text{Mn}_8\text{O}_{16}$  and  $\text{Ag}_{1.8}\text{Mn}_8\text{O}_{16}/\text{rGO}$  hybrids as bifunctional air cathode catalysts at  $20 \text{ mA cm}^{-2}$ . c) Cycling charge-discharge performance of the batteries using Pt/C as the catalyst at  $20 \text{ mA cm}^{-2}$ .

former, about 9% and 10% as opposed to about 10% and 13% for the latter, respectively. Moreover, the zinc-air cell with  $\text{Ag}_{1.8}\text{Mn}_8\text{O}_{16}/\text{rGO}$ -based electrode delivers stable output voltage (no change in charge and discharge voltage) from 90 cycles onwards (Figure 5b). This notable stability is attributed to the decent ORR and OER activities, structural integrity and stability of the  $\text{Ag}_{1.8}\text{Mn}_8\text{O}_{16}/\text{rGO}$  catalyst.

For comparison, a Zn-air cell with commercial Pt/C-based electrode was also cycled under similar conditions. With an initial discharge potential plateau of 1.25 V, similar to that of the cell with  $\text{Ag}_{1.8}\text{Mn}_8\text{O}_{16}/\text{rGO}$ -based electrode, its voltage gap is quickly widened with the cycling. After 10 cycles the charge and discharge voltages already reached the limited of 2.8 and 0.5 V, respectively, signalling the end life of the cell.

The zinc-air cells were also cycled by discharging and charging (10 min each in a cycle) at  $40 \text{ mA cm}^{-2}$  using recurrent galvanic pulses method, and the results are shown in Figure S5. As shown in the Figure S5, the result is similar to Figure 5b and c. The cycling performance of  $\text{Ag}_{1.8}\text{Mn}_8\text{O}_{16}/\text{rGO}$  hybrids is better than that of  $\text{Ag}_{1.8}\text{Mn}_8\text{O}_{16}$  or Pt/C. Due to the polarization effect, all the batteries demonstrate the higher charging potential and the lower discharging potential.<sup>[42]</sup> This unanimously results show the importance of having a catalyst with high stability (e.g.  $\text{Ag}_{1.8}\text{Mn}_8\text{O}_{16}/\text{rGO}$ ) to avoid fast degradation of cell (e.g. with catalysts like Pt/C). The  $\text{Ag}_{1.8}\text{Mn}_8\text{O}_{16}/\text{rGO}$  hybrids are stable after electrochemical test from XRD and SEM results. As shown in Figure S2b and S6, the morphology of the catalyst does not change after electrochemical test, which indicates the catalyst are stable. We also carried out the XRD measurement of the catalyst after electrochemical test. The results are shown in Figure S7. As shown in Figure S7, the two patterns are almost the same, which illustrates the structure of  $\text{Ag}_{1.8}\text{Mn}_8\text{O}_{16}/\text{rGO}$  hybrids is stable. The reasons for battery failure may be caused by the increasing interface resistance rather than the structure collapse of the catalyst.<sup>[43]</sup>

## Conclusion

In summary, a self-assembling approach is used to produce a structurally integrated highly stable air electrode bifunctional catalyst,  $\text{Ag}_{1.8}\text{Mn}_8\text{O}_{16}/\text{rGO}$ . This catalyst shows better onset potential and current density in OER and ORR than that of commercial Pt/C. RDE data suggest 4-electron transfer pathway in ORR of  $\text{Ag}_{1.8}\text{Mn}_8\text{O}_{16}/\text{rGO}$ , which is highly efficient with minimal production of detrimental peroxide species. The high activity and good cycle stability in zinc-air cells may be attributed to the improved electrode conductivity, large surface area, as well as the synergetic coupling effects. With its facile preparation and low cost,  $\text{Ag}_{1.8}\text{Mn}_8\text{O}_{16}/\text{rGO}$  hybrids catalyst promises great potential as ORR/OER bifunctional electrocatalyst for large scale adoption of zinc-air rechargeable battery.

## Experimental Section

### Materials preparation

$\text{Ag}_{1.8}\text{Mn}_8\text{O}_{16}$  nanorods were prepared using hydrothermal method.<sup>[28]</sup> The nanorods were then modified with (3-aminopropyl)-trimethoxysilane (APTMS). The details of preparation for  $\text{Ag}_{1.8}\text{Mn}_8\text{O}_{16}$  nanorods and reduced graphene oxide (rGO) sheets are provided in Supporting Information. The  $\text{Ag}_{1.8}\text{Mn}_8\text{O}_{16}/\text{rGO}$  hybrids were fabricated via self-assembly of APTMS-functionalized  $\text{Ag}_{1.8}\text{Mn}_8\text{O}_{16}$  nanorods and rGO on the basis of electrostatic attraction. In a typical reaction, 24 mg modified  $\text{Ag}_{1.8}\text{Mn}_8\text{O}_{16}$  and 36 mg rGO were dispersed in 20 mL DMF, respectively, denoted as solution A and solution B. Then solution A was added into solution B in a dropwise manner while stirring. The mixed solution was then ultrasonic treated for 60 min at  $0^\circ\text{C}$ . Finally, the composite products were separated from the solution via centrifugation, and thoroughly washed with ethanol.

### Materials characterization

The Zeta potential measurement was carried out on a Zeta potential Analyzer (Malvern ZEN3690). X-ray diffraction (XRD) measurement was performed on an X-ray diffractometer (Bruker D8 GADDS) with Cu K $\alpha$  source ( $\lambda = 0.15406 \text{ nm}$ ) at 40 kV and 30 mA. Scanning electron microscopy (SEM) images were obtained using a JEOL JSM-6700F microscope. The content of Ag, Mn and O element was determined by Oxford INCA Energy Dispersive X-ray (EDX) Spectrometer. Transmission Electron Microscopy (TEM) characterization was performed using a Philips CM300-FEG instrument with operating voltage at 300 kV. X-ray photoelectron spectroscopy (XPS) data were recorded with a Theta Probe electron spectrometer from Thermo Scientific using Al K $\alpha$  ( $h\nu = 1484.6 \text{ eV}$ ) radiation. The binding energies were corrected by the C 1s line at 285.0 eV. The  $\text{N}_2$  adsorption/desorption isotherm was performed on a Quantachrome Autosorb 1-1 C automated adsorption system at liquid nitrogen temperature. The specific surface areas were calculated by a multipoint Braunauer-Emmett-Teller (BET) method. The thermal property was studied by the thermogravimetric analyzer (TGA Q500).

### Electrochemical measurements

Linear sweep voltammetry (LSV) and rotating disk electrode (RDE) measurements were performed on an Autolab potentiostat/galvanostat (PGSTAT302 N) station using a three-electrode system consisting of a Ag/AgCl (in saturated KCl) reference electrode, a Pt foil counter electrode and a glassy carbon working electrode (GC, 5 mm diameter). The working electrode was fabricated by casting Nafion-impregnated catalyst ink onto a glassy carbon disk electrode (5 mm in diameter). For LSV test of different catalysts at 2000 rpm, 10 mg catalyst was dispersed into 1 mL of the 0.5 wt% Nafion solution under sonication to form a catalyst ink. 10  $\mu\text{L}$  of the catalyst ink was deposited on the disk and dried at room temperature. The working electrode was allowed to achieve a catalyst loading of  $0.5 \text{ mg cm}^{-2}$ . The working electrode was immersed in a glass cell containing 0.1 M KOH aqueous electrolyte. A platinum foil and an Ag/AgCl electrode were used as the counter and reference electrodes, respectively. Catalyst activity toward ORR was evaluated in oxygen-saturated electrolyte solution from 0.2 to  $-0.8 \text{ V}$ . The catalytic performance for OER was measured in the electrolyte solution from 0.2 to 1.0 V. The rotation rate is 2000 rpm and the scan rate is  $5 \text{ mV s}^{-1}$ . Commercial Pt/C catalyst (30 wt% platinum on carbon) and other benchmarks were tested using the same procedures.

For RDE test of  $\text{Ag}_{1.8}\text{Mn}_8\text{O}_{16}/\text{rGO}$  hybrids, the catalyst loading was decreased to  $0.1 \text{ mg cm}^{-2}$  in order to reduce the error of electron transfer number. The rotation rate was 400, 625, 900, 1225, 1600 and 2000 rpm, respectively. Catalyst activity toward the ORR was evaluated in oxygen-saturated electrolyte solution from 0.2 to  $-0.8 \text{ V}$  and at a scan rate of  $5 \text{ mV s}^{-1}$ . The number of electrons transferred ( $n$ ) can be calculated by the following Koutecky-Levich equation:<sup>[44]</sup>

$$1/J = 1/J_L + 1/J_K = 1/(B\omega^{1/2}) + 1/J_K \quad (1)$$

$$B = 0.2nFC_0D_o^{2/3}\nu^{-1/6} \quad (2)$$

$$J_K = nFkC_o \quad (3)$$

where  $J$  is the measured current density,  $J_K$  and  $J_L$  are the kinetic- and diffusion- limiting current densities,  $\omega$  is the angular velocity,  $n$  is transferred electron number,  $F$  is the Faraday constant ( $F = 96485 \text{ C mol}^{-1}$ ),  $C_o$  is the bulk concentration of  $\text{O}_2$  in 0.1 M KOH

solution ( $C_0 = 1.2 \times 10^{-6} \text{ mol cm}^{-3}$ ),  $D_0$  is the diffusion coefficient of  $O_2$  in 0.1 M KOH solution ( $D_0 = 1.9 \times 10^{-5} \text{ cm}^2 \text{ s}^{-1}$ ),  $\nu$  is the kinematic viscosity of the electrolyte ( $\nu = 0.01 \text{ cm}^2 \text{ s}^{-1}$ ).

A home-made zinc-air cell device was designed for the battery test. As shown in Figure S8, the air electrode was prepared by spraying the catalyst onto a gas diffusion layer (SGL carbon paper, Germany,  $2 \text{ cm} \times 2 \text{ cm}$ ) to achieve a loading of  $1 \text{ mg cm}^{-2}$ . The electrolyte used in the zinc-air battery was 6 M KOH, and a polished zinc plate ( $7 \text{ cm} \times 6 \text{ cm} \times 0.05 \text{ cm}$ ) was used as the anode. Battery testing and cycling experiments were performed at  $25^\circ \text{C}$  using the recurrent galvanic pulse method, where one cycle consisted of a discharging step ( $20 \text{ mA cm}^{-2}$  for 10 min) followed by a charging step of the same current and duration time.

## Acknowledgements

The authors also acknowledge the financial support from the Advanced Energy Research Programme (IMRE/12-2P0503 and IMRE/12-2P0504), Science and Engineering Research Council (SERC) of A\*STAR (Agency for Science, Technology and Research), Singapore. The authors acknowledge funding support from the Natural Science Foundation of Jiangsu Province (BK20170221).

## Conflict of Interest

The authors declare no conflict of interest.

**Keywords:**  $\text{Ag}_{1.8}\text{Mn}_8\text{O}_{16}/\text{rGO}$  • oxygen reduction reaction • oxygen evolution reaction • bifunctional electrocatalyst • rechargeable zinc-air battery

- [1] J. Fu, R. L. Liang, G. H. Liu, A. P. Yu, Z. Y. Bai, L. Yang, Z. W. Chen, *Adv. Mater.* **2019**, *31*, 1805230.
- [2] A. Noori, M. F. El-Kady, M. S. Rahmanifar, R. B. Kaner, M. F. Mousavi, *Chem. Soc. Rev.* **2019**, *48*, 1272–1341.
- [3] P. Tan, B. Chen, H. R. Xu, H. C. Zhang, W. Z. Cai, M. Ni, M. L. Liu, Z. P. Shao, *Energy Environ. Sci.* **2017**, *10*, 2056–2080.
- [4] X. Ge, A. Sumbaja, D. Wu, T. An, B. Li, F. W. T. Goh, T. S. A. Hor, Y. Zong, Z. Liu, *ACS Catal.* **2015**, *5*, 4643–4667.
- [5] Y. H. Li, Q. Y. Li, H. Q. Wang, L. Zhang, D. P. Wilkinson, J. J. Zhang, *Electrochem. Energy Rev.* **2019**, *2*, 518–538.
- [6] F. Cheng, J. Chen, *Chem. Soc. Rev.* **2012**, *41*, 2172–2192.
- [7] J. S. Lee, S. T. Kim, R. G. Cao, N. S. Choi, M. L. Liu, K. T. Lee, J. Cho, *Adv. Energy Mater.* **2011**, *1*, 34–50.
- [8] J. Wu, H. Yang, *Acc. Chem. Res.* **2013**, *46*, 1848–1857.
- [9] S. Ma, Y. Wu, J. Wang, Y. Zhang, Y. Zhang, X. Yan, Y. Wei, P. Liu, J. Wang, K. Jiang, S. Fan, Y. Xu, Z. Peng, *Nano Lett.* **2015**, *15*, 8084–8090.
- [10] J. Zhang, K. Sasaki, E. Sutter, R. R. Adzic, *Science* **2007**, *315*, 220–222.
- [11] M. Hamdani, R. Singh, P. Chartier, *Int. J. Electrochem. Sci.* **2010**, *5*, 556–577.
- [12] K. Lopez, G. Park, H. J. Sun, J. C. An, S. Eom, J. Shim, *J. Appl. Electrochem.* **2015**, *45*, 313–323.
- [13] X. Wang, F. Rong, F. Huang, P. He, Y. Yang, J. Tang, R. Que, *J. Alloys Compd.* **2019**, *789*, 684–692.
- [14] J. Suntivich, H. A. Gasteiger, N. Yabuuchi, H. Nakanishi, J. B. Goodenough, Y. Shao-Horn, *Nat. Chem.* **2011**, *3*, 546–550.
- [15] M. Yuasa, M. Nishida, T. Kida, N. Yamazoe, K. Shimanoe, *J. Electrochem. Soc.* **2011**, *158*, A605–A610.
- [16] G. Du, X. Liu, Y. Zong, T. S. A. Hor, A. Yu, Z. Liu, *Nanoscale* **2013**, *5*, 4657–4661.
- [17] Y. Su, H. Liu, C. Li, J. Liu, Y. Song, F. Wang, *J. Alloys Compd.* **2019**, *799*, 160–168.
- [18] M. D. Koninck, S. C. Poirier, B. Marsan, *J. Electrochem. Soc.* **2006**, *153*, A2103–A2110.
- [19] W. Xiong, F. Du, Y. Liu, A. J. Perez, M. Supp, T. S. Ramakrishnan, L. Dai, L. Jiang, *J. Am. Chem. Soc.* **2010**, *132*, 15839–15841.
- [20] G. L. Tian, M. Q. Zhao, D. Yu, X. Y. Kong, J. Q. Huang, Q. Zhang, F. Wei, *Small* **2014**, *10*, 2251–2259.
- [21] Z. Lu, W. Xu, J. Ma, Y. Li, X. Sun, L. Jiang, *Adv. Mater.* **2016**, *28*, 7155–7161.
- [22] L. Qu, Y. Liu, J. B. Baek, L. Dai, *ACS Nano* **2010**, *4*, 1321–1326.
- [23] B. Liu, M. Yang, D. Yang, H. Chen, H. Li, *Int. J. Hydrogen Energy* **2018**, *43*, 18270–18278.
- [24] R. Wang, T. Zhou, H. Li, H. Wang, H. Feng, J. Goh, S. Ji, *J. Power Sources* **2014**, *261*, 238–244.
- [25] S. Zhu, Z. Chen, B. Li, D. Higgins, H. Wang, H. Li, Z. Chen, *Electrochim. Acta* **2011**, *56*, 5080–5084.
- [26] J. Chen, X. Tang, J. Liu, E. Zhan, J. Li, X. Huang, W. Shen, *Chem. Mater.* **2007**, *19*, 4292–4299.
- [27] L. Li, D. King, *Chem. Mater.* **2005**, *17*, 4335–4343.
- [28] Y. Sun, X. Hu, W. Zhang, L. Yuan, Y. Huang, *J. Nanopart. Res.* **2011**, *13*, 3139–3148.
- [29] K. S. Novoselov, A. K. Geim, S. V. Morozov, D. Jiang, M. I. Katsnelson, I. V. Grigorieva, S. V. Dubonos, A. A. Firsov, *Nature* **2005**, *438*, 197–200.
- [30] K. I. Bolotin, K. J. Sikes, Z. Jiang, M. Klima, G. Fudenberg, J. Hone, P. Kim, H. L. Stormer, *Solid State Commun.* **2008**, *146*, 351–355.
- [31] J. Liu, J. Tanga, J. J. Gooding, *J. Mater. Chem.* **2012**, *22*, 12435–12452.
- [32] D. Zheng, H. Hu, X. Liu, S. Hu, *Curr. Opin. Colloid Interface Sci.* **2015**, *20*, 383–405.
- [33] Y. Liang, Y. Li, H. Wang, J. Zhou, J. Wang, T. Regier, H. Dai, *Nat. Mater.* **2011**, *10*, 780–786.
- [34] K. Liu, J. Li, Q. Wang, X. Wang, D. Qian, J. Jiang, J. Li, Z. Chen, *J. Alloys Compd.* **2017**, *725*, 260–269.
- [35] Y. Liang, H. Wang, J. Zhou, Y. Li, J. Wang, T. Regier, H. Dai, *J. Am. Chem. Soc.* **2012**, *134*, 3517–3523.
- [36] Q. Shen, J. Yang, K. L. Chen, H. Wang, J. B. Liu, H. Yan, *J. Solid State Electrochem.* **2016**, *20*, 3331–3336.
- [37] H. Huang, Y. Meng, A. Labonte, A. Doble, S. L. Suib, *J. Phys. Chem. C* **2013**, *117*, 25352–25359.
- [38] G. Zhang, L. Zheng, M. Zhang, S. Guo, Z. Liu, Z. Yang, Z. Wang, *Energy Fuels* **2012**, *26*, 618–623.
- [39] M. Prabu, P. Ramakrishnan, S. Shanmugam, *Electrochem. Commun.* **2014**, *41*, 59–63.
- [40] M. Özacar, A. Poyraz, H. Genuino, C. Kuo, Y. Meng, S. L. Suib, *Appl. Catal. A* **2013**, *462*, 64–74.
- [41] T. H. Yang, S. Venkatesan, C. H. Lien, J. L. Chang, J. M. Zen, *Electrochim. Acta* **2011**, *56*, 6205–6210.
- [42] Y. Li, M. Gong, Y. Liang, J. Feng, J. E. Kim, H. Wang, G. Hong, B. Zhang, H. Dai, *Nat. Commun.* **2013**, *4*, 1805–1811.
- [43] E. Davari, D. G. Ivey, *Sustain. Energy Fuels* **2018**, *2*, 39–67.
- [44] B. Li, X. Ge, F. W. T. Goh, T. S. A. Hor, D. Geng, G. Du, Z. Liu, J. Zhang, X. Liu, Y. Zong, *Nanoscale* **2015**, *7*, 1830–1838.

Manuscript received: August 12, 2021  
Revised manuscript received: September 7, 2021  
Accepted manuscript online: September 8, 2021  
Version of record online: September 23, 2021